Delft University of Technology

Energy Cascade Phenomena in Temporal Boundary Layers

Cimarelli, Andrea; Boga, Gabriele; Pavan, Anna; Costa, Pedro; Stalio, Enrico

RESEARCH

Energy Cascade Phenomena in Temporal Boundary Layers

Andrea Cimarelli[1] · Gabriele Boga[1] · Anna Pavan[1] · Pedro Costa[2] · Enrico Stalio[1]

Abstract
The geometrically complex mechanisms of energy transfer in the compound space of scales and positions of wall turbulent flows are investigated in a temporally evolving boundary layer. The phenomena consist of spatially ascending reverse and forward cascades from the small production scales of the buffer layer to the small dissipative scales distributed among the entire boundary layer height. The observed qualitative behaviour conforms with previous results in turbulent channel flow, thus suggesting that the observed phenomenology is a robust statistical feature of wall turbulence in general. An interesting feature is the behaviour of energy transfer at the turbulent/non-turbulent interface, where forward energy cascade is found to be almost absent. In particular, the turbulent core is found to sustain a variety of large-scale wall-parallel motions at the turbulent interface through weak but persistent reverse energy cascades. This behaviour conforms with previous results in free shear flows, thus suggesting that the observed phenomenology is a robust statistical feature of turbulent shear flows featuring turbulent/non-turbulent interfaces in general.

✉ Andrea Cimarelli
andrea.cimarelli@unimore.it

Gabriele Boga
gabriele.boga@unimore.it

Anna Pavan
anna.pavan@unimore.it

Pedro Costa
p.simoescosta@tudelft.nl

Enrico Stalio
enrico.stalio@unimore.it

1   Department of Engineering "Enzo Ferrari", University of Modena and Reggio Emilia, Via Vivarelli 10, 41125 Modena, Italy

2   Process and Energy Department, TU Delft, Leeghwaterstraat 39, Delft 2628 CB, The Netherlands

1 Introduction

Due to its relevance, wall turbulence has been the subject of many studies over the years, see Smits et al. (2011) for a partial review. Paradigmatic flows have been channels, pipes and turbulent boundary layers. Such flows represent the simplest kind of wall-bounded flows, thus allowing for a detailed analysis of the physical mechanisms underlying more complex real-world problems. With respect to channels and pipes, boundary layers are characterized by additional phenomena related with the presence of a free boundary and, hence, of a turbulent/non-turbulent interface (da Silva et al. 2014). This makes the study of boundary layers of a more general relevance for industrial and geophysical problems. However, the spatial inhomogeneity in the streamwise direction renders boundary layers more challenging for simulations in comparison with streamwise-homogeneous channels and pipes. Tied with this streamwise inhomogeneity is indeed the need for applying proper inflow and tripping conditions (leading to very long domains) or rescaling and recycling methods to circumvent the simulation of transition, further complicating the computational approach (Schlatter and Örlü 2010; Lund et al. 1998). A method to avoid all these issues is to consider a temporally rather than spatially evolving boundary layer. As recently shown in Kozul et al. (2016), the temporal boundary layer presents similar statistical features but its ease of set-up and computational cost savings make it an attractive setting to study the physics of turbulent boundary layers.

The recovery of statistical homogeneity in the streamwise direction for temporal boundary layers has important advantages concerning the suitability of statistical tools used to understand the physics of the flow and to develop models. A significant example is given by statistical observables addressing the multi-dimensional and multi-scale features of the flow such as energy spectra and second-order structure functions (Alexakis and Biferale 2018). These quantities and the related budget equations allow to address relevant physical phenomena of turbulence such as the energy cascade in the space of scales from the production to the dissipation eddies. However, in the presence of non-homogeneous directions, the two statistical approaches suffer from some critical issues. In particular, the energy spectrum cannot be defined in the inhomogeneous (and therefore non-periodic) directions, and hence the dimensionality of the multiscale features of the flow that can be analysed must be reduced to the sole statistical homogeneous directions, see e.g. Mizuno (2016), Cho et al. (2018), Lee and Moser (2019), Chan et al. (2021) and Wang et al. (2021). The budget equation for the second-order structure function also called generalized Kolmogorov equation (Hill 2002) does not suffer from such constraint since two-point statistics are defined also in inhomogeneous directions. Hence, the multiscale features of turbulence can be always characterized in the full three-dimensional space of scales. Indeed, the problem of the presence of statistically inhomogeneous directions is of opposite nature with respect to spectral energy equations, being at the basis of an increase in the dimensionality of the problem to be analysed. Indeed, each inhomogeneous direction introduces a related spatial flux. Accordingly, in the case of fully inhomogeneous flows, the equation of second-order structure functions is characterized by a field of fluxes in a 6-dimensional space, the three-dimensional space of scales plus the three-dimensional space of positions, thus challenging for a rational approach of analysis and for a clear understanding of the highlighted physics.

In this context, the adoption of a temporal rather than spatially evolving boundary layer allows us to reduce the statistical inhomogeneous directions to the sole wall distance. On one side, the second-order structure function problem is reduced to 4 dimensions (the 3-dimensional space of scales plus wall distance) while, on the other, the spectral energy

equation can be used to address also the space of streamwise scales. In other words, the statistical symmetries of both approaches recover those of channels and pipes. The purpose of the present work is to study the multi-scale features of boundary layers and, in accordance with the previous reasoning, we will use the theoretical framework provided by the generalized Kolmogorov equation when applied to temporal flows. A similar analysis has been already performed in Yao et al. (2022) for a spatially developing boundary layer undergoing bypass transition. Particular attention will be devoted to the study of the reverse energy cascade mechanisms (Piomelli et al. 1991; Domaradzki et al. 1994; Härtel et al. 1994; Jiménez 1999; Dunn and Morrison 2005) that are known to play a key role in the self-sustaining cycles of turbulence (Cimarelli et al. 2013, 2016) and in the entrainment mechanisms at the interface (Cimarelli et al. 2015, 2021). In the flow settings of a turbulent boundary layer, these two phenomena are simultaneously occurring and dominate the dynamics of the near-wall (the former) and outer regions (the latter). To put the present setup in perspective, we will start by assessing the degree of similarity of the flow statistics of the temporal boundary layer with respect to classical results in the main fields of investigation commonly pursued in wall turbulence. The analysis of the energy cascade will then follow.
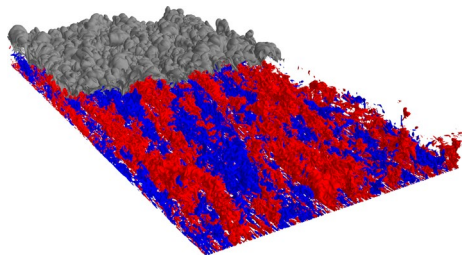
2 Direct Numerical Simulation

The temporal boundary layer consists in a moving wall at constant speed U_w at the bottom ($z = 0$) of an initially quiescent fluid. A view of the instantaneous pattern taken by the flow field is reported in Fig. 1 and of the temporal evolution of the flow is shown in Fig. 2. The design of the simulation follows the seminal work of Kozul et al. (2016) to which the reader is referred for further details. Here, we limit the description to the main numerical and flow settings. To achieve transition to turbulence, an initial condition for the streamwise velocity field is assigned,

$$U_0(z, 0) = \left(1 + c'\right) \frac{U_w}{2} \left\{ 1 + \tanh\left[\frac{D}{2\theta}\left(1 - \frac{z}{D}\right)\right] \right\}. \tag{1}$$

The initial velocity profile is designed to mimic the wake of a wall-mounted trip wire with diameter D commonly used in wind tunnel experiments to trigger turbulence. Accordingly, $\theta = 54\nu/U_w$ can be thought of as the momentum thickness of the associated shear layer. Superimposed to this initial condition, a white noise $c'(x, y, z) \in [-0.05, 0.05]$ is used to speed up transition. No-slip and impermeable boundary condition representing a moving wall is imposed at the bottom boundary, while a free-slip impermeable boundary condition is imposed at the top. Periodic boundary conditions are imposed in the streamwise and

Fig. 1 Instantaneous isosurfaces of enstrophy $\Omega = 0.1\langle\Omega\rangle_w$ (grey) and low and high velocity fluctuations (blue and red respectively) $u = \pm 0.1 U_w$. Here, $\langle\Omega\rangle_w(t)$ is the time-dependent average value of enstrophy at the wall
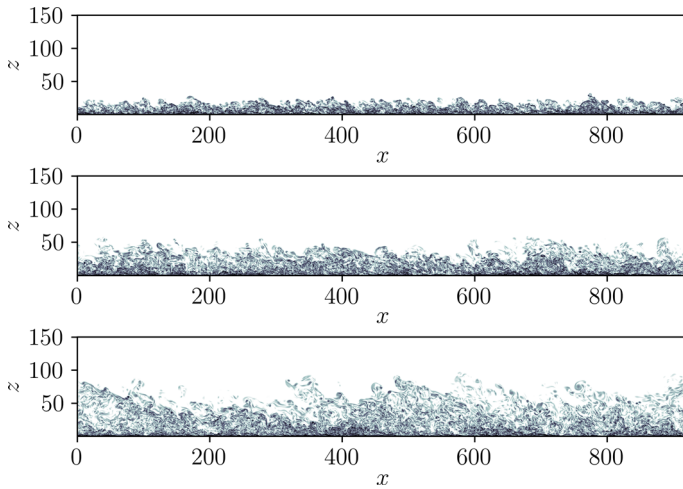
Fig. 2 Direct Numerical Simulation of a temporal boundary layer. Instantaneous patterns taken by the spanwise vorticity at three different evolution times corresponding to $Re_\tau = 500, 1000$ and 1500 from top to bottom

spanwise directions. The Navier–Stokes equations have been solved using the massively-parallel open-source code CaNS Costa (2018), which uses a standard pressure-projection method with the spatial discretization based on a staggered second-order finite-difference scheme. A mixed time integration method is adopted. Indeed, to avoid the very small time step demanded by the highly stretched grid along the wall-normal direction, the diffusion terms in the vertical direction are integrated in time implicitly using a Crank-Nicholson scheme. On the other hand, all the other terms of the equations are integrated explicitly with a three-step Runge–Kutta method using the 95% of the stability margin ($CFL = 0.95$).

The adopted numerical domain has dimensions $(L_x, L_y, L_z) = (924D, 462D, 220D)$, and has been discretized using $(N_x, N_y, N_z) = (3072, 3072, 768)$ points. The size of the domain is determined by the target final boundary layer thickness δ_f that, in turn, dictates the largest friction Reynolds number of the simulation $Re_\tau = u_\tau \delta_f / \nu$. Following Kozul et al. (2016), we consider $\delta_f / L_z = 1/3$ and the domain dimensions are defined in order to reach $Re_\tau = 1500$ at the end of the simulation. This choice for the domain size ensures that confinement effects at the final simulation time are negligible. In contrast to the domain dimensions, the grid spacing is determined by the smallest value of the friction length that occurs at an early stage of the simulation when skin friction reaches its maximum, see Fig. 3. Even at this worst condition, the number of points used leads to a very good resolution that in friction units reads $(\Delta x^+, \Delta y^+, \Delta z_w^+) = (8.73, 4.37, 0.13)$. The grid stretching uses a standard error function clustering, with a clustering parameter $\alpha_z = 2.25$ (see Chapter 2 in Orlandi (2000)). For the reader's convenience, the domain size as a function of the boundary layer thickness and the grid resolution as a function of the viscous length for three different times of evolution corresponding to $Re_\tau = 500, 1000$ and 1500 are reported in Table 1.

Statistics are computed by performing a spatial average in the statistically homogeneous wall-parallel directions and an ensemble average between four independent simulations obtained by varying the noise seed in the initial condition. The corresponding average operator will be hereafter denoted as $\langle \cdot \rangle$. The customary Reynolds decomposition will

Table 1 Domain size and grid resolution for three different times of evolution corresponding to $Re_\tau = 500$, 1000 and 1500.

Re_τ	$(L_x, L_y, L_z)/\delta$	Δx^+	Δy^+	Δz_w^+	Δz_δ^+	$\Delta z_\delta/\eta$
500	42.48, 19.58, 10.14	6.74	3.37	0.10	4.23	0.66
1000	18.53, 9.26, 4.42	6.06	3.03	0.09	7.10	0.95
1500	11.87, 5.93, 2.83	5.80	2.90	0.09	9.17	1.13

Δz_w and Δz_δ are the wall-normal spacing evaluated at the wall and at the boundary layer thickness and η is the corresponding local Kolmogorov length
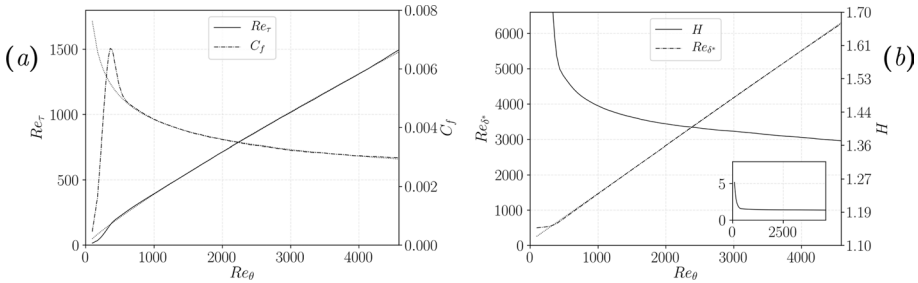

Fig. 3 **a** Evolution of the friction coefficient c_f (dashed line) and of the friction Reynolds number Re_τ (solid line) as a function of the Reynolds number based on the momentum thickness, Re_θ. In the fully-developed region ($Re_\theta > 900$), these quantities are well fitted by $Re_\tau \approx 0.93 Re_\theta^{7/8}$ and $c_f \approx 0.024 Re_\theta^{-1/4}$, which are depicted in the dotted lines. **b** Evolution of displacement thickness Reynolds number Re_{δ^*} and of the shape factor H as a function of the Reynolds number based on the momentum thickness Re_θ (note that $H = Re_{\delta^*}/Re_\theta$)

be adopted and the corresponding average and fluctuating velocities will be denoted as $u_i^* = U_i + u_i$ where $U_i = \langle u_i^* \rangle$ and u_i^* is the total velocity field. Here, x, y and z (u, v and w) denote the streamwise, spanwise and wall-normal directions (velocities).

3 Main Flow Features

Despite its potential in the study of wall turbulence, the temporal boundary layer has been the subject of a rather small number of investigations, see e.g. Kozul et al. (2016), Watanabe et al. (2018) and Kozul et al. (2020). In order to clarify the role that this flow configuration can have in improving our current understanding of wall turbulence, selected topics commonly pursued in this field of research will be addressed.

We start by addressing the temporal evolution of a few important integral quantities. More specifically, Fig. 3a reports the evolution of the friction coefficient c_f and of the friction Reynolds number Re_τ as functions of the momentum thickness Reynolds number $Re_\theta = U_w \theta / \nu$. Interestingly, it appears that the classical relation $c_f \sim Re_\theta^{-1/4}$ commonly observed in experiments and DNS of spatially-developing turbulent boundary layers Schlichting and Kestin (1961); Schlatter et al. (2010) with a scaling factor of about $0.024 - 0.026$, is nicely followed. From the classical scaling in zero pressure gradient turbulent boundary layers, it also follows that $Re_\tau \sim Re_\theta^{7/8}$ and, indeed, our results also feature this almost linear relation between the two quantities with a scaling factor of 0.93.

Note that this is also very close to the fit $Re_\tau \approx 1.13 Re_\theta^{0.843}$ provided in Schlatter and Örlü (2010). Figure 3b shows the evolution of the displacement thickness Reynolds number $Re_{\delta^*} = U_w \delta^*/\nu$ and of the shape factor $H = \delta^*/\theta$ again as a function of the momentum thickness Reynolds number Re_θ. Once more, the evolution of H closely follows the trend observed in spatially-developing boundary layers at these Reynolds numbers; see Monkewitz et al. (2007). While redundant, the corresponding evolution of Re_{δ^*} is displayed there to illustrate the growth of the displacement thickness, as the slope of this curve is precisely the shape factor $H = Re_{\delta^*}/Re_\theta$.

In Fig. 4a the mean velocity profiles at different Reynolds numbers are shown, along with the standard diagnostic function $\Xi(z) \equiv z^+ dU^+/dz^+$ which may be used to estimate the von Kármán constant κ when evaluated in the overlap region. It is worth pointing out that streamwise velocity is shifted by the wall velocity U_w in order to produce the customary view of wall turbulence. Naturally, the linear relation $u^+ = z^+$ provides a good approximation up to $z^+ \approx 5$, as in all canonical wall-bounded turbulent flows. For sufficiently high Reynolds numbers, the overlap region can be approximated with the relation $u^+ = 1/\kappa \ln\left(y^+\right) + B$. By using the plateau shown by the diagnostic function in the overlap layer, we estimate $\kappa = 0.436$ that would lead to a constant $B = 5.75$. These values are found to fit reasonably well the mean velocity profile in the lower part of the overlap layer, $40 < z^+ < 0.1 Re_\tau$ where, as expected, the diagnostic function used to evaluate the von Kármán constant shows the plateau. To note that by using values for the constants obtained from literature on turbulent boundary layers Marusic et al. (2010), $\kappa = 0.384$ and $B = 4.173$, a reasonably good fitting of the mean velocity profile is still observed but for $120 < z^+ < 0.16 Re_\tau$, i.e. the range of validity is shifted toward the external part of the overlap layer. Overall, the presence of a sufficiently wide overlap layer is evident from the mean velocity profile for the highest Reynolds number case. The consequent separation of scales is apparent also in the profiles of the Reynolds shear stress $-\langle uw \rangle$ reported in Fig. 4b. Indeed, the expected high-Reynolds number asymptotic limit for the Reynolds shear stresses, $-\langle uw \rangle = u_\tau^2$, is found to be approached at the highest Reynolds number considered.

In Fig. 5a the contributions from each velocity component to the turbulence intensity are shown as a function of the wall distance and for three Reynolds numbers. The typical behaviour of wall turbulence is observed. It consists in a buffer layer where the highest
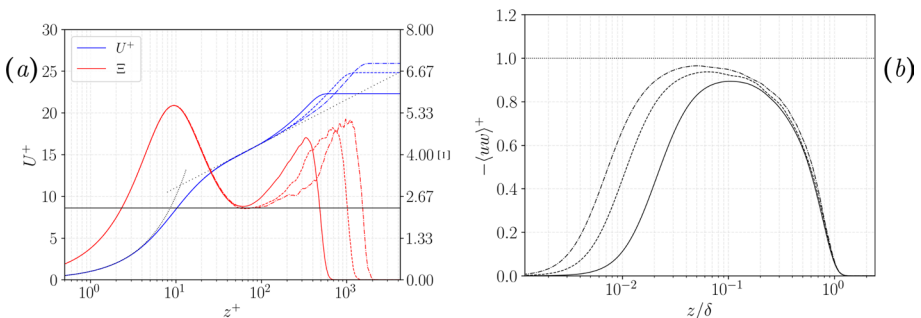

Fig. 4 **a** Profiles of the mean velocity $U^+(z^+)$ (blue lines) and of the diagnostic function Ξ (red lines) for three different evolution times corresponding to $Re_\tau = 500$ (solid), 1000 (dashed) and 1500 (dashed dotted). **b** Profile of Reynolds shear stresses compared with u_τ^2. for three different evolution times corresponding to $Re_\tau = 500$ (solid), 1000 (dashed) and 1500 (dashed dotted)
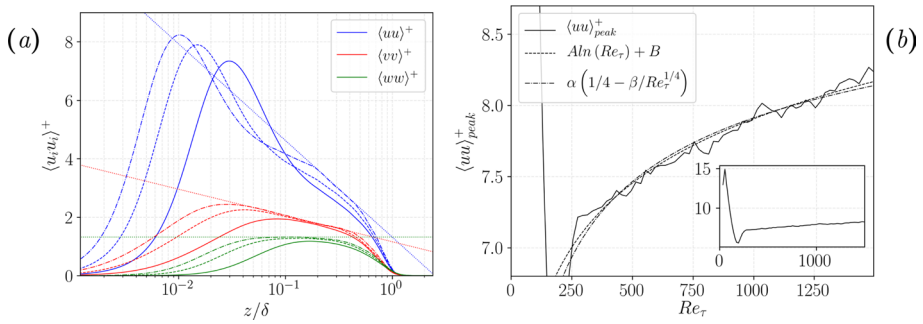
Fig. 5 **a** Profiles of turbulence intensities for three different evolution times corresponding to $Re_\tau = 500$ (solid), 1000 (dashed) and 1500 (dashed dotted). The scaling laws for the overlap layer, Eq. (3), are reported with dotted lines with fitting parameters $B_1 = 1.32$ and $A_1 = 1.435$, $B_2 = 1.16$ and $A_2 = 0.39$ and $B_3 = 1.32$. **b** Reynolds number dependence of the inner peak value of the streamwise turbulence intensity $\langle u'u' \rangle^+_{peak}$. The scaling laws (2) are also reported

turbulence activity is concentrated and in streamwise velocity fluctuations that largely exceed in intensity those in the wall-parallel directions. An important subject of debate in this context is the violation of the inner scaling of near-wall turbulence. It consists in a Reynolds number dependence of near-wall quantities that are otherwise thought to be universal when scaled with kinematic viscosity ν and wall shear stress τ_w, i.e with u_τ for velocities and ν/u_τ for lengths. This universality has been widely verified for the mean flow but not for the Reynolds stresses. Indeed, as shown in Fig. 5a, an increase of the intensity of the streamwise and spanwise velocity fluctuations near the wall is observed by increasing the Reynolds number. In this respect, two scaling laws have been proposed in order to compensate the behaviour with Reynolds of the streamwise turbulence intensity peak $\langle uu \rangle^+_{peak}$,

$$\langle u^2 \rangle^+_{peak} = A \ln (Re_\tau) + B,$$
$$\langle u^2 \rangle^+_{peak} = \alpha \left(1/4 - \beta Re_\tau^{-1/4} \right) \tag{2}$$

The first logarithmic scaling can be explained by inner-outer interaction between near-wall and outer eddies (Marusic et al. 2017) while the second power-law scaling on the constraint provided to dissipation by the maximum asymptotic value of turbulence production Chen and Sreenivasan (2021). The behaviour of these two scaling law is similar for low and intermediate Reynolds numbers but different in the limit of very high Reynolds numbers. Accordingly, the data of the temporal boundary layer can be reasonably fitted by both the two scaling laws due to the intermediate values of Reynolds number investigated as shown in Fig. 5b. The fitting parameters are measured to be $A = 0.65$ and $B = 3.40$ for the logarithmic scaling law and $\alpha = 41.11$ and $\beta = 0.324$ for the power law. These values are close with those found in the literature for more classical wall-bounded flows, $A = 0.63$, $B = 3.80$, $\alpha = 46$ and $\beta = 0.42$.

Another important aspect regarding turbulent intensities that deserves more attention is their behaviour in the overlap layer. According to the Townsend's original work (Townsend 1976), the overlap layer can be conceived as an equilibrium layer of constant shear stress equal to ρu_τ^2 (see Fig. 4b) where turbulence production and dissipation almost balance (see Sect. §4.1) and populated by a hierarchy of self-similar eddies attached to the wall so that their characteristic lengths are proportional to the distance from the wall. These simple

arguments are expected to apply for asymptotically high Reynolds numbers and are at the basis of the so-called attached eddy model (Marusic and Monty 2019). The success of this model is its capability on giving a physical explanation to several statistical features of wall turbulence and, more importantly, on providing quantitative predictions on turbulence in the overlap layer. An example is given by the scaling laws for the turbulence intensities

$$
\begin{aligned}
\langle u^2 \rangle^+ &= B_1 - A_1 \ln(z/\delta), \\
\langle v^2 \rangle^+ &= B_2 - A_2 \ln(z/\delta), \\
\langle w^2 \rangle^+ &= B_3
\end{aligned}
\tag{3}
$$

These laws have found strong support from experimental and numerical data at high Reynolds numbers, see Marusic and Monty (2019) and references therein, and are found to be satisfied also by the temporal boundary layer although the Reynolds number considered are not high. Indeed, as shown in Fig. 5a, the scaling laws for the spanwise and wall-normal fluctuations appears to be satisfied in the overlap layer. The resulting coefficients are respectively $B_2 = 1.16$, $A_2 = 0.39$ and $B_3 = 1.32$. A scaling law is observed also for the streamwise velocity fluctuations. However, the range of wall distances covered goes beyond the overlap layer and the measured coefficients, $B_1 = 1.32$ and $A_1 = 1.435$, are significantly different from those reported in literature ($B_1 = 2.39$ and $A_1 = 1.03$). Hence, we argue that this perceived logarithmic region does not pertain to the attached eddy scaling laws.

An additional prediction of the attached eddy hypothesis is a scaling law also for the turbulent spectra in the overlap layer. As shown in Nikora (1999), the superposition of Kolmogorov's like energy cascades triggered by eddies whose size is proportional to the wall distance within an equilbrium layer where production follows the law of the wall and balances dissipation, leads to the following scaling of the energy spectra,

$$
\begin{aligned}
E_{uu}(k_x) &\sim u_\tau^2 \, k_x^{-1} && \text{for} \quad \frac{1}{\delta} < k_x < \frac{1}{z} \\
E_{uu}(k_x) &\sim \left(\frac{u_\tau^3}{\kappa z} \right)^{2/3} k_x^{-5/3} && \text{for} \quad k_x > \frac{1}{z}
\end{aligned}
\tag{4}
$$

where E_{uu} is the energy spectrum of streamwise velocity fluctuations and k_x is the streamwise wavenumber. Hence, for scales smaller than the wall distance the classical $k_x^{-5/3}$ inertial scaling is expected to hold, while for scales of the order of the wall distance and larger, the effect of the mean shear leads to a k_x^{-1} scaling. As shown in Fig. 6, these scaling laws are found to fit the behaviour of energy spectra within the overlap region of the simulated temporal boundary layer especially for the two higher Reynolds number cases. As expected, the cross-over between the two scaling laws is well represented by the wall distance, i.e. the wavenumber $1/z$.

4 Flow of Energy in the Compound Space of Scales and Positions

We address now the self-sustaining processes of turbulence in the temporal boundary layer from an energetic point of view. We will first characterize the spatial inhomogeneity of the flow by analysing the turbulent kinetic energy budget and then we will extend this description by addressing the scale-by-scale properties of the phenomena involved through the
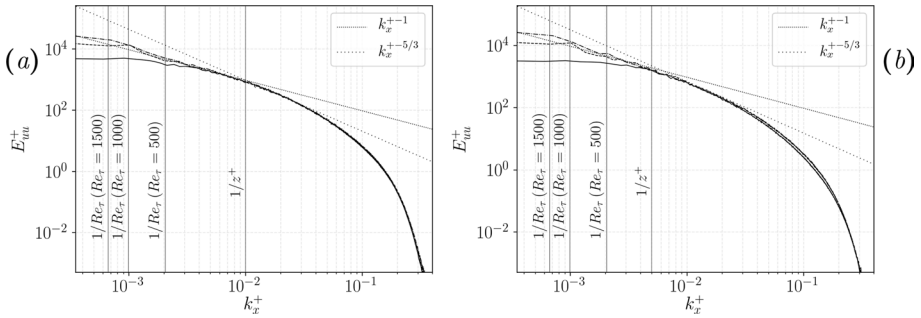
Fig. 6 One-dimensional longitudinal spectra of streamwise velocity fluctuations $E_{uu}(k_x)$ evaluated at $z^+ = 100$ (**a**) and $z^+ = 200$ (**b**) for three different evolution times corresponding to $Re_\tau = 500$ (solid), 1000 (dashed) and 1500 (dashed dotted). The shear-dominated and the inertia-dominated scaling laws, Eq. (4), are reported with solid and dashed lines respectively. The vertical lines denote the cross-over scale z and the boundary layer thickness δ in friction units

analysis of the generalized Kolmogorov equation. In what follows, the inner region of the flow will be considered as composed by a viscous sublayer for $z^+ < 5$, by a buffer layer for $5 < z^+ < 60$ and by an overlap layer for $60 < z^+ < 0.2Re_\tau$. The rest of the flow will be called outer region $0.2Re_\tau < z^+ < Re_\tau$ which involve also the interface region for $z^+ \approx Re_\tau$. The main energetic processes characterizing these flow regions is reported in the following section.

4.1 The Turbulent Kinetic Energy Equation

The budget of turbulent kinetic energy allows for a quantitative description of the distinctive processes governing the different flow regions. In other words, it integrates in a simple way the overall multidimensional behaviour of turbulence by describing the energetics only in physical space. For the symmetries of the temporal boundary layer, the equation reads

$$\frac{\partial \langle k \rangle}{\partial t} + \frac{\partial \psi}{\partial z} = -\langle uw \rangle \frac{\partial U}{\partial z} - \langle \epsilon \rangle \tag{5}$$

where $k = u_i u_i / 2$ is the turbulent kinetic energy, $\epsilon = \nu(\partial u_i / \partial x_j)(\partial u_i / \partial x_j)$ is the turbulent pseudo-dissipation rate and

$$\psi = \langle kw \rangle + \frac{1}{\rho}\langle pw \rangle - \nu \frac{\partial \langle k \rangle}{\partial z} \tag{6}$$

is the spatial flux along different flow regions. Equation (5) shows that the spatial flux is driven by an extended source term given by the balance of turbulence production and dissipation plus the time variation of the local turbulent kinetic energy content, i.e.

$$\frac{\partial \psi}{\partial z} = s(z) \tag{7}$$

with the extended source term defined as

$$s(z) = -\frac{\partial \langle k \rangle}{\partial t} - \langle uw \rangle \frac{\partial U}{\partial z} - \langle \epsilon \rangle \tag{8}$$

As shown in Fig. 7a, the extended source s^+ identifies the buffer layer region (say $5 < z^+ < 60$) as the engine of turbulence and the viscous sublayer (say $z^+ < 5$) as the main sink. In particular, the peak value $s^+_{max} = 0.11$ is located at $z^+ = 11$ in close agreement with the behaviour observed in channel flows (Cimarelli et al. 2015). In accordance with Eq. (7), the spatial flux is found to diverge from the peak of the extended source in the buffer layer to feed both the wall ($\psi < 0$) and the flow at higher wall distances ($\psi > 0$). By increasing the wall distance, the flux directed towards higher wall distances is continuously enriched by the action of the extended source term and reaches a peak value at $z^+ \approx 35$. Indeed, from $z^+ > 35$ the spatial flux starts to decrease (hence, to release energy) due to the extended source term becoming negative. This decrease is interrupted when entering the overlap layer (say $60 < z^+ < 0.2Re_\tau$) and outer region (say $z^+ > 0.2Re_\tau$) where the extended source term exhibits a second outer region of source. As better shown by the enlargement reported in Fig. 7b, the extended source term exhibits an outer positive source that—although weaker than that in the near-wall region—is expected to become dominant for high Reynolds numbers; see Cimarelli et al. (2015). Indeed, the outer source scales in mixed units as the overlap and outer regions containing it. More specifically, we measure that its extension roughly is $100 < z^+ < 0.55Re_\tau$ for the three Reynolds numbers considered thus highlighting that by increasing the Re_τ its integral contribution to the overall source of turbulence increases and might exceed that near the wall that on the contrary is almost invariant with Re_τ. An accompanying feature of the outer energy source is the increase of the spatial flux intensity. This spatial flux is indeed energized by the outer source and reaches a second peak intensity roughly at the end of the outer source at $z^+ \approx 0.55Re_\tau$. In accordance with the increase of the integral contribution of the outer source with Re_τ, the second peak intensity of the spatial flux is found to increase with Re_τ. After this peak, the spatial flux decreases and releases its energy thus sustaining turbulence at higher wall distances until it vanishes in the external region of the boundary layer. Indeed, for $z^+ > 0.55Re_\tau$ the extended source is always negative thus dissipating the energy provided by the spatial flux. It is worth notice that the spatial flux remains active ($\psi \neq 0$) for wall distances significantly larger than that identified by the interface at $z^+ = Re_\tau$. Indeed, fluctuations of the velocity field persists in the external region of the boundary layer. For sufficiently high wall distances, $z^+ \gg Re_\tau$, these fluctuations are the result of non-local phenomena of displacement of otherwise quiescent fluid performed by the large-scale structures populating the
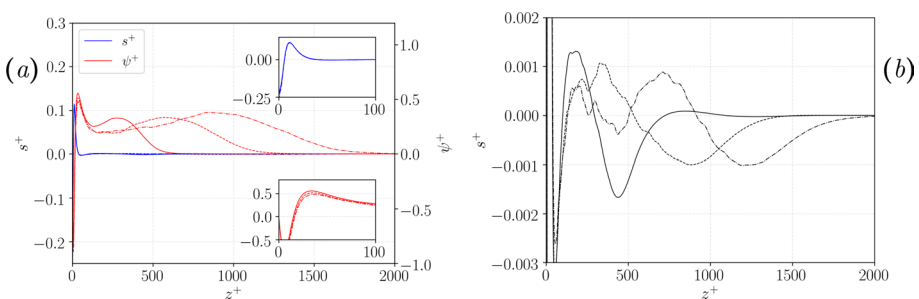

Fig. 7 **a** Extended source $s^+(z^+)$ and spatial flux $\psi^+(z^+)$ of turbulent kinetic energy for three different evolution times corresponding to $Re_\tau = 500$ (solid), 1000 (dashed) and 1500 (dashed dotted). The two insets report an enlarged view of the near-wall behaviour. **b** Enlarged view of the second-outer source of turbulent kinetic energy

turbulent core of the boundary layer, see Cimarelli et al. (2021) for analogous considerations in the external region of a turbulent jet. Accordingly, the fluctuations of the external region are non-turbulent and irrotational in nature and the spatial flux feeding them is non-diffusive in nature, $\psi \approx \langle kw \rangle + \langle pw \rangle / \rho$.

The overall behaviour of the kinetic energy budget qualitatively conforms to more classical results from channel and pipe flows, see e.g. Bernardini et al. (2014), Lee and Moser (2015) and Pirozzoli et al. (2021). An interesting feature associated with the presence of the outer source of turbulent kinetic energy is its possible connection with the anomalous scaling of near-wall quantities already described in the previous Sect. §3, see Fig. 5b. As conjectured in Cimarelli et al. (2015) for turbulent channels, the idea is that the emergence of an increasingly large outer source of kinetic energy with Re_τ leads to a reduction of the intensity of the spatial fluxes leaving the near-wall region to feed the outer turbulent fluctuations. In other words, the repulsive effect of the outer source represents an increasing confinement effect with Re_τ of the spatial flux emerging from the wall thus leading to a sort of near-wall accumulation of turbulent kinetic energy with Re_τ. As shown in the inset of Fig. 7a, the decrease of peak intensity of the spatial flux leaving the near-wall region is a further supporting evidence of this scenario also for boundary layers.

4.2 The Generalized Kolmogorov Equation

The generalized Kolmogorov equation Hill (2002) represents a sufficiently general statistical formalism to address the multi-dimensional cascade processes of turbulence from production to dissipation (Danaila et al. 2001; Marati et al. 2004; Burattini et al. 2005; Rincon 2006; Togni et al. 2015; Portela et al. 2017; Hamba 2018; Mollicone et al. 2018; Hamba 2019; Gatti et al. 2020; Zimmerman et al. 2022; Chiarini et al. 2022). The equation is based on the second-order structure function of the fluctuating velocity field $\langle \delta q^2 \rangle \equiv \langle \delta u_i \delta u_i \rangle$ where $\delta u_i \equiv u_i(\boldsymbol{x}', t) - u_i(\boldsymbol{x}'', t)$ is the fluctuating velocity increment. Hereafter, we will often refer to the second-order structure function as the scale energy even if such an interpretation is somewhat arguable especially in inhomogeneous flows for large separations, see the reasoning provided in Cimarelli et al. (2016) and the possible alternative expressions derived in Hamba (2018). For the symmetries of a temporal evolving turbulent boundary layer, the second-order structure function depends on a 5-dimensional space $\langle \delta q^2 \rangle = \langle \delta q^2 \rangle (r_x, r_y, r_z, z_c, t)$ and the equation reads

$$
\frac{\partial \langle \delta q^2 \rangle}{\partial t} + \frac{\partial \langle \delta q^2 \delta u_i \rangle}{\partial r_i} + \frac{\partial \langle \delta q^2 \delta U \rangle}{\partial r_x} - 2v \frac{\partial^2 \langle \delta q^2 \rangle}{\partial r_i \partial r_i} +
$$
$$
\frac{\partial \langle \delta q^2 \widetilde{w} \rangle}{\partial z_c} + \frac{2}{\rho} \frac{\partial \langle \delta p \delta w \rangle}{\partial z_c} - \frac{v}{2} \frac{\partial^2 \langle \delta q^2 \rangle}{\partial z_c^2} =
$$
$$
-2 \langle \delta u \delta w \rangle \widetilde{\left(\frac{dU}{dz} \right)} - 2 \langle \delta u \, \widetilde{w} \rangle \, \delta \left(\frac{dU}{dz} \right) - 4 \langle \widetilde{\epsilon} \rangle
$$

$$(9)$$

where $\boldsymbol{r} = \boldsymbol{x}' - \boldsymbol{x}''$ is the two-point separation vector, $\boldsymbol{x}_c = (\boldsymbol{x}' + \boldsymbol{x}'')/2$ is the position vector of the mid-point and $\widetilde{\cdot}$ denotes the two-point average.

For obvious reasons of visualization, we will limit the analysis to the three-dimensional space (r_x, r_y, z_c) for $r_z = 0$ and for a time t corresponding to $Re_\tau = 1500$. In the $r_z = 0$

hyper-plane of the augmented space of turbulence, the conservative form of Eq. (9) can be written as,

$$\frac{\partial \phi_{r_\pi}}{\partial r_\pi} + \frac{\partial \phi_{c_z}}{\partial z_c} = \zeta \tag{10}$$

where $\pi = 1, 2$ denotes the statistically homogeneous streamwise and spanwise directions and ζ is an extended source term that together with production and dissipation takes into account also the time variation of the local scale-energy content and the scale-energy exchange with the $r_z \neq 0$-space,

$$\zeta = -\frac{\partial \langle \delta q^2 \rangle}{\partial t} - 2 \langle \delta u \delta w \rangle \widetilde{\left(\frac{dU}{dz} \right)} - 4 \langle \epsilon \rangle - \frac{\partial \phi_{r_z}}{\partial r_z} \tag{11}$$

where $\phi_{r_z} = \langle \delta q^2 \delta w \rangle - 2\nu \partial \langle \delta q^2 \rangle / \partial r_z$. The conservative form (10) highlights that the generalized Kolmogorov equation represents an exact and formally precise formalism for the study of the cascade processes in the space of wall-parallel scales through the flux

$$\phi_{r_\pi} = \langle \delta q^2 \delta u_\pi \rangle - 2\nu \frac{\partial \langle \delta q^2 \rangle}{\partial r_\pi} \tag{12}$$

and the flow of scale energy between different flow regions through the spatial flux

$$\phi_c = \langle \delta q^2 \widetilde{w} \rangle + \frac{2}{\rho} \langle \delta p \delta w \rangle - \frac{\nu}{2} \frac{\partial \langle \delta q^2 \rangle}{\partial z_c} \tag{13}$$

from the production to the dissipation regions of the hyper-plane $r_z = 0$ of the augmented space of turbulence identified by ζ.

The near-wall behaviour of the cascade and spatial fluxes of scale energy in the turbulent boundary layer at $Re_\tau = 1500$ are reported in Fig. 8a. The streamlines of the flux field are colored with the extended source term ζ that, in accordance with Eq. (10), denotes the amount of scale-energy locally drained ($\zeta > 0$) and released ($\zeta < 0$) by fluxes. The field of fluxes takes origin from a singularity point $(r_x^+, r_y^+, z_c^+) = (0, 70, 16)$ located well within the near-wall scale-energy source region (green iso-surface). The fluxes are energized by the near-wall source (see the streamlines color) and diverges feeding both longer and wider fluctuations before bending towards the wall and towards the bulk of the flow. By considering the branch of fluxes towards the bulk, a spiraling behaviour consisting of spatially ascending reverse and forward cascades is observed in agreement with results first reported in Cimarelli et al. (2013) for channel flows and confirmed by Yao et al. (2022) for boundary layers undergoing bypass transition. The behaviour consists of reverse cascades intercepting longer and wider structures away from the wall followed by a forward cascade feeding the small-scale range at still higher wall distances where scale energy is eventually dissipated.

By extending the analysis to larger scales and higher wall distances, the presence of an outer scale-energy source becomes evident. As shown in Fig. 8b, the field of fluxes feeding the z_c-distributed small-scale dissipative sink in the outer region of the flow are strongly influenced by the outer source of scale energy (orange iso-surface). In particular, the field of fluxes emerging from the near-wall region is found to be energized by the outer source (see the streamlines color) and within it further diverges feeding even longer and wider structures before eventually converging towards smaller scales.

Fig. 8 Source and fluxes of scale energy in the near-wall (**a**) and outer (**b**) regions of the turbulent boundary layer at $Re_\tau = 1500$. The scale-energy paths $(\phi_{r_x}, \phi_{r_y}, \phi_{c_z})$ are colored with ζ^+ and the scale-energy source $\xi^+ = 0.46$ and $\xi^+ = 0.01$ are reported with a green and orange iso-surface, respectively
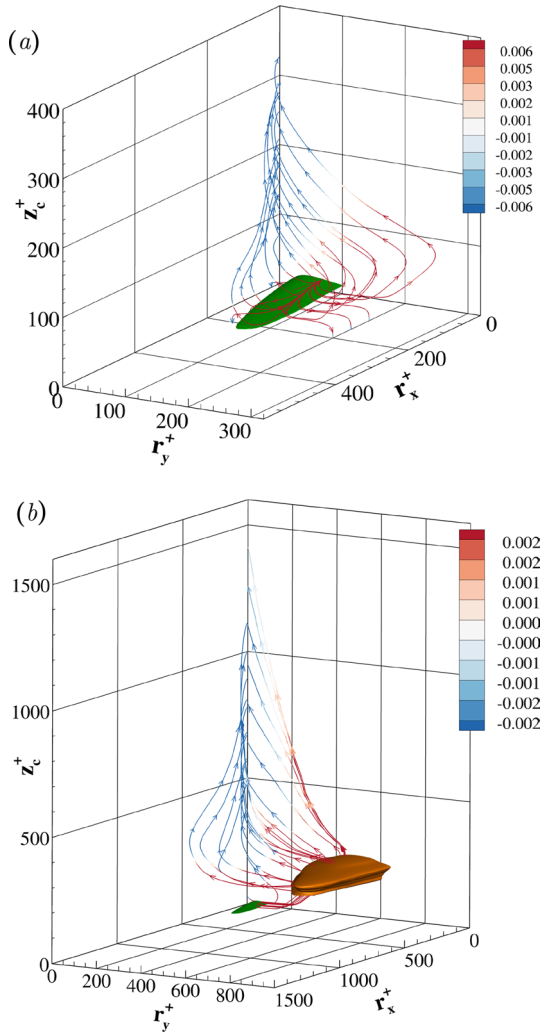
Compared with the near-wall source peak located at $(r_x^+, r_y^+, z_c^+) = (0, 40, 11)$ with intensity $\xi_{inn}^+ = 0.73$, the peak value of the outer source is weaker $\xi_{inn}^+ = 0.014$ and involves significantly larger scales $(r_x^+, r_y^+, z_c^+) = (0, 0.26Re_\tau, 0.1Re_\tau)$.

In the framework of wall-bounded flows, the peculiarity of boundary layers is the presence of entrainment phenomena at the edge of the boundary layer itself. The field of fluxes that feeds this region of the flow is shown in Fig. 9. Similar to the family of fluxes feeding the z_c-distributed dissipative range of small scales of the outer region, the branch of fluxes feeding the interface is energized by the outer scale-energy source (see the streamlines color). Again a divergent pattern of the flux streamline is observed towards longer and wider structures but, in this case, it is not followed by convergence towards the small scales. Instead, the field of fluxes is almost aligned with the z_c-direction with a small but non-negligible reverse cascade both in the streamwise and spanwise scales. In other words, the turbulent core of the boundary layer is found to sustain a variety of large wall-parallel

Fig. 9 Branch of scale-energy fluxes towards the interface dissipative sink of the turbulent boundary layer at $Re_\tau = 1500$. The scale-energy paths $(\phi_{r_x}, \phi_{r_y}, \phi_{c_z})$ are colored with ζ^+ and the scale-energy source $\xi^+ = 0.46$ and $\xi^+ = 0.01$ are reported with a green and orange iso-surface, respectively
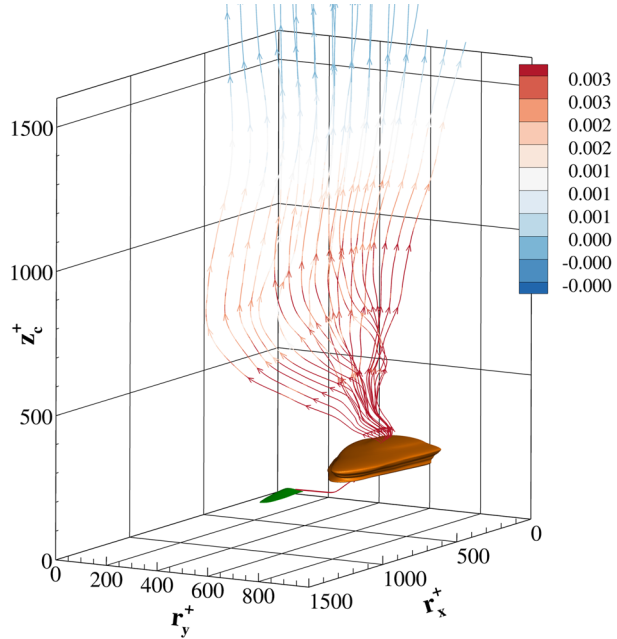
structures at the boundary layer interface. Interestingly, this phenomenology is fully consistent with recent findings on the turbulent/non-turbulent interface of free shear flows reported in Cimarelli et al. (2015), Zhou and Vassilicos (2020) and Cimarelli et al. (2021).

5 Conclusions

The Kolmogorov's groundbreaking intuition was to reduce the complex problem of turbulence to its essential phenomena by assuming homogeneity and isotropy at high Reynolds numbers. In these conditions, the prominent feature of turbulence is the energy cascade from large to small scales which is governed by a single scalar quantity, the average dissipation rate. However, actual turbulent flows have a much richer physics, involving, beyond energy cascade, anisotropic turbulent production and inhomogeneous spatial fluxes. Such processes are strongly scale and position dependent and lead to a geometrically complex redistribution of energy. This is a distinct feature of wall turbulence where turbulence production is located amid the spectrum of scales near the wall to feed longer and wider turbulent structures in the bulk of the flow. These phenomena have been classically studied in the statistical settings of turbulent channels. Here, we investigate their behaviour for the symmetries of temporal boundary layer. Contrary to channels and pipes, the distinguishing feature of boundary layer is the presence of entrainment phenomena at their edge.

Direct numerical simulations of a temporal boundary layer up to $Re_\tau = 1500$ have been performed. We have shown that the statistical features of the flow are very similar to that of spatially evolving boundary layers. In particular, relevant issues commonly investigated in wall turbulence have been addressed and found to agree and in some cases extend the present knowledge given by spatially evolving flows. The choice of a temporally rather than spatially evolving boundary layer has been dictated by the recovery of statistical

homogeneity in the streamwise direction. Such property is indeed recognized to be crucial for a clear understanding of the complex multi-dimensional features of energy transfer. The analysis of the generalized Kolmogorov equation revealed that the overall behaviour of energy transfer from the near-wall production to the small dissipative scales of the bulk of the flow is qualitatively not markedly different with respect to previous results in wall turbulence. It consists of spatially ascending reverse cascades taking origin from the small production scales of the buffer layer and sustaining longer and wider structures at larger wall distances, followed by a still ascending forward cascade towards small scales where eventually dissipation occurs. An interesting feature is observed in the interface region. It consists of a dissipative layer fed by fluxes taking origin from the buffer layer and energized by the outer sourcing mechanisms of the overlap layer. The peculiarity of the interface region is that forward cascade processes are almost absent in the space of wall-parallel scales. Only a weak but persistent reverse cascade survives at the interface, thus supporting the idea that a variety of large wall-parallel scales are sustained by the turbulent core at the boundary layer interface.

Author Contributions AC wrote the main manuscript text. GB prepared Figures 1, 2, 3, 4, 5, 6 and 7, AC prepared Figures 8, 9. GB preformed the simulations. PC, AP and GB designed the numerical settings for the simulations and performed preliminary runs. All authors reviewed the manuscript.

Data availability Data available on request from the authors

References

Alexakis, A., Biferale, L.: Cascades and transitions in turbulent flows. Phys. Rep. **767**, 1–101 (2018)

Bernardini, M., Pirozzoli, S., Orlandi, P.: Velocity statistics in turbulent channel flow up to $re_\tau = 4000$. J. Fluid Mech. **742**, 171–191 (2014)

Burattini, P., Antonia, R.A., Danaila, L.: Scale-by-scale energy budget on the axis of a turbulent round jet. J. Turb. **6**, 19 (2005)

Chan, C., Schlatter, P., Chin, R.C.: Interscale transport mechanisms in turbulent boundary layers. J. Fluid Mech. **921**, 13 (2021)

Chen, X., Sreenivasan, K.R.: Reynolds number scaling of the peak turbulence intensity in wall flows. J. Fluid Mech. **908**, 3 (2021)

Chiarini, A., Mauriello, M., Gatti, D., Quadrio, M.: Ascending–descending and direct-inverse cascades of Reynolds stresses in turbulent couette flow. J. Fluid Mech. **930**, 9 (2022)

Cho, M., Hwang, Y., Choi, H.: Scale interactions and spectral energy transfer in turbulent channel flow. J. Fluid Mech. **854**, 474–504 (2018)

Cimarelli, A., De Angelis, E., Casciola, C.M.: Paths of energy in turbulent channel flows. J. Fluid Mech. **715**, 436–451 (2013)

Cimarelli, A., Cocconi, G., Frohnapfel, B., De Angelis, E.: Spectral enstrophy budget in a shear-less flow with turbulent/non-turbulent interface. Phys. Fluids **27**(12), 125106 (2015)

Cimarelli, A., De Angelis, E., Schlatter, P., Brethouwer, G., Talamelli, A., Casciola, C.M.: Sources and fluxes of scale energy in the overlap layer of wall turbulence. J. Fluid Mech. **771**, 407–423 (2015)

Cimarelli, A., De Angelis, E., Jiménez, J., Casciola, C.M.: Cascades and wall-normal fluxes in turbulent channel flows. J. Fluid Mech. **796**, 417–436 (2016)

Cimarelli, A., Mollicone, J.-P., Van Reeuwijk, M., De Angelis, E.: Spatially evolving cascades in temporal planar jets. J. Fluid Mech. **910**, 19 (2021)

Costa, P.: A FFT-based finite-difference solver for massively-parallel direct numerical simulations of turbulent flows. Comput. Math. Appl. **76**(8), 1853–1862 (2018)

da Silva, C.B., Hunt, J.C.R., Eames, I., Westerweel, J.: Interfacial layers between regions of different turbulence intensity. Annu. Rev. Fluid Mech. **46**, 567–590 (2014)

Danaila, L., Anselmet, F., Zhou, T., Antonia, R.A.: Turbulent energy scale budget equations in a fully developed channel flow. J. Fluid Mech. **430**, 87–109 (2001)

Domaradzki, J.A., Liu, W., Härtel, C., Kleiser, L.: Energy transfer in numerically simulated wall-bounded turbulent flows. Phys. Fluids **6**(4), 1583–1599 (1994)

Dunn, D.C., Morrison, J.F.: Analysis of the energy budget in turbulent channel flow using orthogonal wavelets. Comput. Fluids **34**(2), 199–224 (2005)

Gatti, D., Chiarini, A., Cimarelli, A., Quadrio, M.: Structure function tensor equations in inhomogeneous turbulence. J. Fluid Mech. **898**, 5 (2020)

Hamba, F.: Turbulent energy density in scale space for inhomogeneous turbulence. J. Fluid Mech. **842**, 532–553 (2018)

Hamba, F.: Inverse energy cascade and vortical structure in the near-wall region of turbulent channel flow. Phys. Rev. Fluids **4**(11), 114609 (2019)

Härtel, C., Kleiser, L., Unger, F., Friedrich, R.: Subgrid-scale energy transfer in the near-wall region of turbulent flows. Phys. Fluids **6**(9), 3130–3143 (1994)

Hill, R.J.: Exact second-order structure-function relationship. J. Fluid Mech. **468**, 317–326 (2002)

Jiménez, J.: The physics of wall turbulence. Phys. A Stat. Mech. App. **263**(1–4), 252–262 (1999)

Kozul, M., Chung, D., Monty, J.P.: Direct numerical simulation of the incompressible temporally developing turbulent boundary layer. J. Fluid Mech. **796**, 437–472 (2016)

Kozul, M., Hearst, R.J., Monty, J.P., Ganapathisubramani, B., Chung, D.: Response of the temporal turbulent boundary layer to decaying free-stream turbulence. J. Fluid Mech. **896**, 11 (2020)

Lee, M., Moser, R.D.: Direct numerical simulation of turbulent channel flow up to $Re_\tau \approx 5200$. J. Fluid Mech. **774**, 395–415 (2015)

Lee, M., Moser, R.D.: Spectral analysis of the budget equation in turbulent channel flows at high Reynolds number. J. Fluid Mech. **860**, 886–938 (2019)

Lund, T.S., Wu, X., Squires, K.D.: Generation of turbulent inflow data for spatially-developing boundary layer simulations. J. Comput. Phys. **140**(2), 233–258 (1998)

Marati, N., Casciola, C.M., Piva, R.: Energy cascade and spatial fluxes in wall turbulence. J. Fluid Mech. **521**, 191–215 (2004)

Marusic, I., Monty, J.P.: Attached Eddy model of wall turbulence. Annu. Rev. Fluid Mech. **51**, 49–74 (2019)

Marusic, I., McKeon, B.J., Monkewitz, P.A., Nagib, H.M., Smits, A.J., Sreenivasan, K.R.: Wall-bounded turbulent flows at high reynolds numbers: recent advances and key issues. Phys. Fluids **22**(6), 065103 (2010)

Marusic, I., Baars, W.J., Hutchins, N.: Scaling of the streamwise turbulence intensity in the context of inner-outer interactions in wall turbulence. Phys. Rev. Fluids **2**(10), 100502 (2017)

Mizuno, Y.: Spectra of energy transport in turbulent channel flows for moderate reynolds numbers. J. Fluid Mech. **805**, 171–187 (2016)

Mollicone, J.-P., Battista, F., Gualtieri, P., Casciola, C.M.: Turbulence dynamics in separated flows: the generalised kolmogorov equation for inhomogeneous anisotropic conditions. J. Fluid Mech. **841**, 1012–1039 (2018)

Monkewitz, P.A., Chauhan, K.A., Nagib, H.M.: Self-consistent high-Reynolds-number asymptotics for zero-pressure-gradient turbulent boundary layers. Phys. Fluids **19**(11), 115101 (2007)

Nikora, V.: Origin of the "- 1" spectral law in wall-bounded turbulence. Phys. Rev. Lett. **83**(4), 734 (1999)

Orlandi, P.: Fluid Flow Phenomena: A Numerical Toolkit vol. 55. Springer, (2000)

Piomelli, U., Cabot, W.H., Moin, P., Lee, S.: Subgrid-scale backscatter in turbulent and transitional flows. Phys. Fluids A **3**(7), 1766–1771 (1991)

Pirozzoli, S., Romero, J., Fatica, M., Verzicco, R., Orlandi, P.: One-point statistics for turbulent pipe flow up to $re_\tau \approx 6000$. J. Fluid Mech. **926**, 28 (2021)

Portela, F.A., Papadakis, G., Vassilicos, J.C.: The turbulence cascade in the near wake of a square prism. J. Fluid Mech. **825**, 315–352 (2017)

Rincon, F.: Anisotropy, inhomogeneity and inertial-range scalings in turbulent convection. J. Fluid Mech. **563**, 43–69 (2006)

Schlatter, P., Örlü, R.: Assessment of direct numerical simulation data of turbulent boundary layers. J. Fluid Mech. **659**, 116–126 (2010)

Schlatter, P., Li, Q., Brethouwer, G., Johansson, A.V., Henningson, D.S.: Simulations of spatially evolving turbulent boundary layers up to Re = 4300. Int. J. Heat Fluid Flow **31**, 251–261 (2010)

Schlichting, H., Kestin, J.: Boundary Layer Theory vol. 121. Springer (1961)

Smits, A.J., McKeon, B.J., Marusic, I.: High-reynolds number wall turbulence. Annu. Rev. Fluid Mech. **43**, 353–375 (2011)

Togni, R., Cimarelli, A., De Angelis, E.: Physical and scale-by-scale analysis of rayleigh-bénard convection. J. Fluid Mech. **782**, 380–404 (2015)

Townsend, A.A.R.: The Structure of Turbulent Shear Flow. Cambridge University Press, Cambridge (1976)

Wang, W., Pan, C., Wang, J.: Energy transfer structures associated with large-scale motions in a turbulent boundary layer. J. Fluid Mech. **906**, 14 (2021)

Watanabe, T., Zhang, X., Nagata, K.: Turbulent/non-turbulent interfaces detected in dns of incompressible turbulent boundary layers. Phys. Fluids **30**(3), 035102 (2018)

Yao, H., Mollicone, J.-P., Papadakis, G.: Analysis of interscale energy transfer in a boundary layer undergoing bypass transition. J. Fluid Mech. **941**, 14 (2022)

Zhou, Y., Vassilicos, J.C.: Energy cascade at the turbulent/nonturbulent interface. Phys. Rev. Fluids **5**(6), 064604 (2020)

Zimmerman, S.J., Antonia, R.A., Djenidi, L., Philip, J., Klewicki, J.C.: Approach to the 4/3 law for turbulent pipe and channel flows examined through a reformulated scale-by-scale energy budget. J. Fluid Mech. **931**, 28 (2022)